Matter

Article

Accelerated chemical space search using a quantum-inspired cluster expansion approach

Hitarth Choubisa, Jehad Abed, Douglas Mendoza, ..., Brandon R. Sutherland, Alán Aspuru-Guzik, Edward H. Sargent

alan@aspuru.com (A.A.-G.)
ted.sargent@utoronto.ca (E.H.S.)

Highlights

Mapping chemical space search to Ising model enables accurate and efficient search

Significant speed-up over genetic algorithm, bayesian optimization, and commercial solver

Development of electronic structure proxy to predict in-laboratory catalyst performance

Discovery of $RuCrMnSbO_2$, which is stable and efficient for acidic oxygen evolution

Chemical space search is a challenging problem, given the large size of the chemical space and complex structure-property relationship. In this work, we propose a solution by mapping the task of optimizing material property to that of finding the ground state of an Ising model. In our benchmarking, we observe significant time acceleration using a quantum-inspired device. Applying this to discovery of catalyst, we discover a new stable and efficient quaternary oxide catalyst for acidic oxygen evolution reaction.

Benchmark 2
First qualification/assessment of material properties and/or performance

Matter

CellPress

Article

Accelerated chemical space search using a quantum-inspired cluster expansion approach

Hitarth Choubisa,[1,10] Jehad Abed,[1,10] Douglas Mendoza,[2,3] Hidetoshi Matsumura,[4] Masahiko Sugimura,[4] Zhenpeng Yao,[2,3,6] Ziyun Wang,[1,5] Brandon R. Sutherland,[1] Alán Aspuru-Guzik,[6,7,8,9,*] and Edward H. Sargent[1,11,*]

SUMMARY

To enable the accelerated discovery of materials with desirable properties, it is critical to develop accurate and efficient search algorithms. Quantum annealers and similar quantum-inspired optimizers have the potential to provide accelerated computation for certain combinatorial optimization challenges. However, they have not been exploited for materials discovery because of the absence of compatible optimization mapping methods. Here, by combining cluster expansion with a quantum-inspired superposition technique, we lever quantum annealers in chemical space exploration for the first time. This approach enables us to accelerate the search of materials with desirable properties 10–50 times faster than genetic algorithms and bayesian optimizations, with a significant improvement in ground state prediction accuracy. We apply this to the discovery of acidic oxygen evolution reaction catalysts and find a promising previously unexplored chemical family of Ru-Cr-Mn-Sb-O_2. The best catalyst shows a mass activity eight times higher than state-of-the-art RuO_2 and maintains performance for 180 h.

INTRODUCTION

Finding materials with desirable properties such as high d-band centers, high stability, high mobilities, optimal bandgaps, or low overpotentials to enable efficient energy harvesting,[1] catalysis,[2] light emission,[3] sensing,[4] and more is a challenging high-order optimization problem. Traditionally, density functional theory (DFT)-based screening[5,6] has been used to explore chemical space. However, the high computational cost associated with DFT calculations[7] and the vastness of chemical space[8] make exhaustive searches infeasible. To predict material properties rapidly, studies in recent years have employed machine learning (ML)-based surrogate models.[9–13] Among them, approaches based on learning from stoichiometries[14,15] and generative models such as variational autoencoders (VAEs)[7,16–18] and generative adversarial networks (GANs)[19–22] allow accurate property prediction without DFT relaxation, which is a computationally expensive step. However, despite the presence of an accurate ML model, chemical exploration can still be limited because of the generation of infeasible structures by generative models, absence of efficient search strategies, and large chemical space (see Note S1 for an estimate). Therefore, ensuring global optimization across an exhaustive search within chemical space is difficult with such methods. This is further complicated by the observation that formulating the chemical space search as an optimization problem is itself challenging due to the absence of a simple analytic optimization expression and the non-convex nature of structure-property relationships due to the presence of multiple local minima.[23,24]

PROGRESS AND POTENTIAL

Searching the chemical space exhaustively is difficult because of its large size and non-convex structure-property relationship, preventing discovery of optimal alloys and doped materials. Here, we develop a method that maps the search for materials with optimal properties to that of finding the ground state of an Ising model. This enables the use of specialized combinatorial optimization devices such as the quantum annealers and quantum-inspired optimizers, resulting in an efficient and accurate search. We apply this to the discovery of acidic oxygen evolution reaction catalysts and discover a previously unreported stable and efficient catalyst demonstrated through in-laboratory experiments. We envision that this approach will be used to further explore diverse and more complex alloyed structures that were previously difficult to explore because of computational complexity and that this method will provide a way to test usefulness of various computing architectures to demonstrate computational advantage.

CellPress

Matter
Article

We aim to address this challenge by developing a new method to search chemical space by reframing the problem as one of finding the Ising Hamiltonian's ground state (Figure 1). Our method maps the cluster expansion (CE)[25,26] formulation to an Ising model. This mapping enables potential use of quantum annealers and quadratic unconstrained binary optimization (QUBO) solvers to perform rapid global searches in chemical space. We choose a quantum-inspired optimization engine (Digital Annealer[27] [DA]; refer to the methods section "DA" for more details) as the choice to solve for the ground state of our Ising model. Our choice is inspired by the fact that DA has been shown to efficiently find ground states of Ising models.[28,29] We term the approach quantum-inspired CE (QCE). When used on its own, QCE allows us to circumvent the DFT relaxation process and simultaneously enable us to accelerate the search for materials that optimize target properties of interest (Figure 1). At the same time, QCE can also be used in conjunction with superior property prediction models such as interatomic potentials[10,30,31] that can accurately predict the properties to exhaustively search the material space and find materials with desirable properties.

In this paper, we first detail the QCE method and benchmark it by finding stable materials in the quaternary Cu-Ni-Pd-Ag chemical system. Following the benchmark, we lever the framework to find stable and efficient acidic oxygen evolution reaction (OER) catalysts by developing an experimentally verified quantum mechanical catalyst efficiency proxy. Finally, we verify our predictions experimentally and our top catalyst (a never-before-reported multi-metal oxide) demonstrates best-in-class stability among all acidic rutile OER catalysts with overpotentials <250 mV.

RESULTS

Mapping CE to Ising Hamiltonian instance

CEs are power series expansions of the partition function that account for many-body interactions. They have been widely employed for the exploration of materials.[26,32–36] In CE, the desired property P is expressed as a function of the 3D arrangement of atoms in the lattice. The 3D arrangement of atoms can be mapped bijectively to a configuration vector $\sigma = [\sigma_1, \sigma_2, ..., \sigma_N]$ where σ_i represents the type of atom at a specific lattice site i. N is the total number of sites in the lattice. The property of interest P is expressed as a function of the vector σ:

$$P(\sigma) = \sum_f J_f \Pi_f(\sigma) \qquad \text{(Equation 1)}$$

where J_f is the fitted correlation coefficient and $\Pi_f(\sigma)$ is the correlation function of multi-body interaction terms σ. By expanding the correlation functions in Equation 1, we get:

$$P(\sigma) = \sum_{i \in cluster\_1} J_f \langle \Phi_i(\sigma_i) \rangle_f + \sum_{i,j \in cluster\_2} J_f \langle \Phi_i(\sigma_i) \cdot \Phi_j(\sigma_j) \rangle_f$$
$$+ \sum_{i,j,k \in cluster\_3} J_f \langle \Phi_i(\sigma_i) \cdot \Phi_j(\sigma_j) \cdot \Phi_k(\sigma_k) \rangle_f + ... \qquad \text{(Equation 2)}$$

where $\Phi_i(\sigma_i)$ is an orthogonal basis function dependent on the atom type . σ_i[35] Terms *cluster_1*, *cluster_2*, and *cluster_3* are single-body, two-body, and three-body interactions of a unique cluster of sites. The J_f coefficients are obtained by fitting the CE on the DFT-generated data (initial structures and relaxed structure properties)[36–38] (Figure S1B). The CE is an infinite series, but it can be approximated as a finite series.[38,39]

The key step of our proposed mapping is expressing the basis functions $\varphi_i(\sigma_i)$ as a superposition of all basis functions for every site within the lattice:

[1]Department of Electrical and Computer Engineering, University of Toronto, 10 King's College Road, Toronto, ON M5S 3G4, Canada

[2]Department of Chemistry, University of Toronto, 80 St. George Street, Toronto, ON M5S 3H6, Canada

[3]Department of Chemistry and Chemical Biology, Harvard University, 12 Oxford Street, Cambridge, MA 02138, USA

[4]Fujitsu Consulting (Canada) Inc, Toronto, ON, Canada

[5]School of Chemical Sciences, The University of Auckland, Auckland 1010, New Zealand

[6]Chemical Physics Theory Group, Department of Chemistry, University of Toronto, Toronto, ON M5S 3H6, Canada

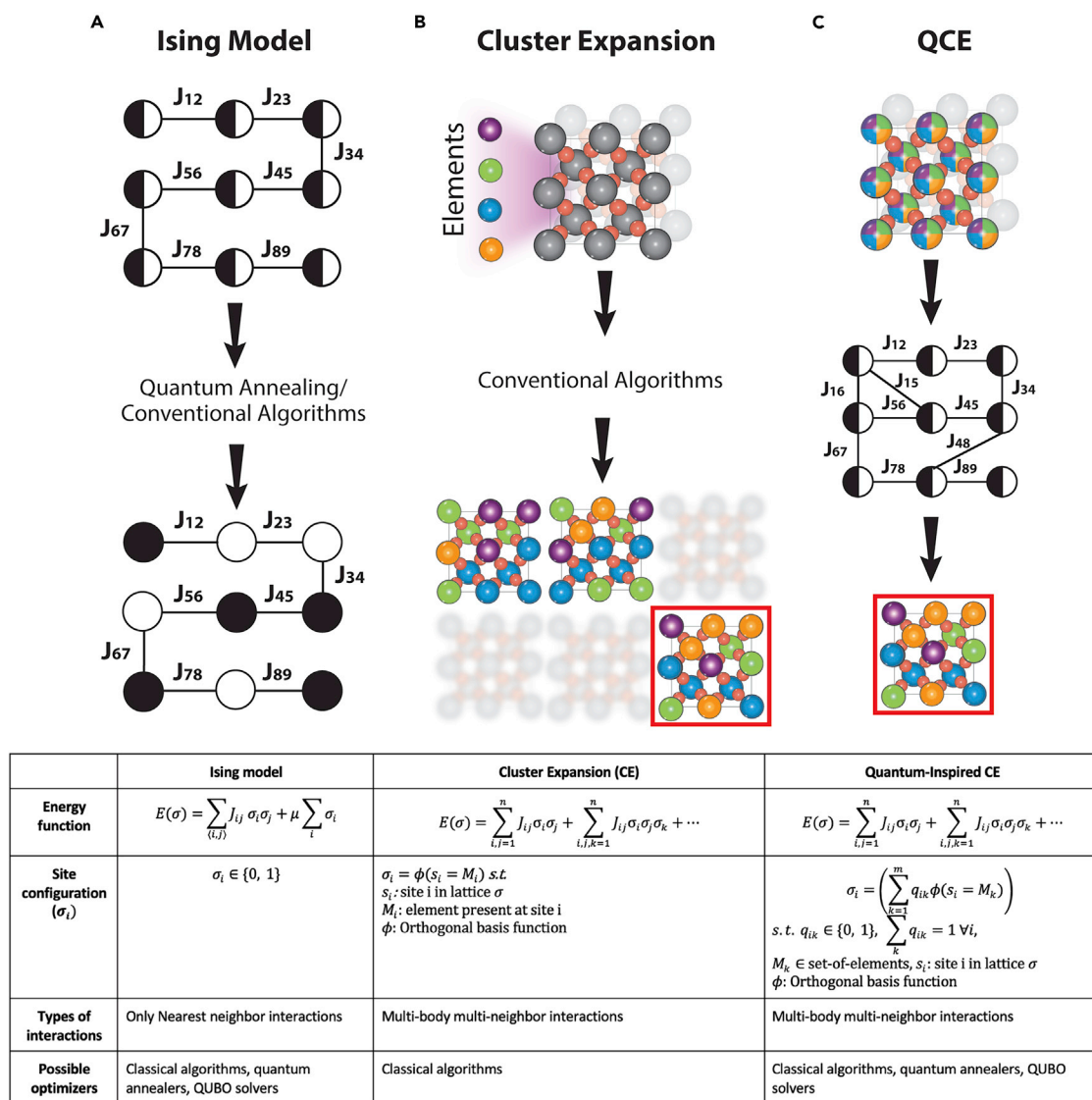[7]Department of Computer Science, University of Toronto, Toronto, ON M5S 3H6, Canada

[8]Vector Institute for Artificial Intelligence, Toronto, ON M5S 1M1, Canada

[9]Lebovic Fellow, Canadian Institute for Advanced Research, Toronto, ON M5S 1M1, Canada

[10]These authors contributed equally

[11]Lead contact

*Correspondence: alan@aspuru.com (A.A.-G.), ted.sargent@utoronto.ca (E.H.S.)

CellPress

A **Ising Model**

J_{12} J_{23} J_{34} J_{56} J_{45} J_{67} J_{78} J_{89}

Quantum Annealing/
Conventional Algorithms

J_{12} J_{23} J_{34} J_{56} J_{45} J_{67} J_{78} J_{89}

B **Cluster Expansion**

Elements

Conventional Algorithms

C **QCE**

J_{12} J_{23} J_{16} J_{15} J_{34} J_{56} J_{45} J_{67} J_{48} J_{78} J_{89}

	Ising model	Cluster Expansion (CE)	Quantum-Inspired CE
Energy function	$E(\sigma) = \sum_{\langle i,j \rangle} J_{ij}\,\sigma_i \sigma_j + \mu \sum_i \sigma_i$	$E(\sigma) = \sum_{i,j=1}^{n} J_{ij}\,\sigma_i \sigma_j + \sum_{i,j,k=1}^{n} J_{ij}\,\sigma_i \sigma_j \sigma_k + \cdots$	$E(\sigma) = \sum_{i,j=1}^{n} J_{ij}\,\sigma_i \sigma_j + \sum_{i,j,k=1}^{n} J_{ij}\,\sigma_i \sigma_j \sigma_k + \cdots$
Site configuration (σ_i)	$\sigma_i \in \{0, 1\}$	$\sigma_i = \phi(s_i = M_i)\ s.t.$ s_i: site i in lattice σ M_i: element present at site i ϕ: Orthogonal basis function	$\sigma_i = \left(\sum_{k=1}^{m} q_{ik} \phi(s_i = M_k) \right)$ $s.t.\ q_{ik} \in \{0, 1\}, \sum_k q_{ik} = 1\ \forall i,$ $M_k \in$ set-of-elements, s_i: site i in lattice σ ϕ: Orthogonal basis function
Types of interactions	Only Nearest neighbor interactions	Multi-body multi-neighbor interactions	Multi-body multi-neighbor interactions
Possible optimizers	Classical algorithms, quantum annealers, QUBO solvers	Classical algorithms	Classical algorithms, quantum annealers, QUBO solvers

Figure 1. Mapping chemical space search to finding the ground state of an Ising model with QCE

Comparison of the Ising model (first column: A), CE (second column: B), and our proposed approach (third column: C). Ising models are computational models of ferroelectricity. Various optimizers, including quantum annealers, quantum-inspired optimizers, as well as conventional algorithms such as Metropolis, can be used to find ground state of Ising models. On the other hand, CEs are used for solving the combinatorial search problem in chemical space, but only conventional algorithms have been used so far for exploring CE. As part of this paper, we propose a mapping (third column of inset table) from CE to an Ising model. This enables us to lever the same set of optimizers for CE as those are available for finding ground state of Ising models.

$$\Phi_i(\sigma_i) = \sum_{j=1}^{n} c(M_j) \cdot \varphi_i(\sigma_i = M_j)$$

$$\sum_{j=1}^{n} c(M_j) = 1 \qquad \text{(Equation 3)}$$

$$c(M_j) \in \{0, 1\} \ \forall \ j$$

such that $c(M_j)$ is the linear combination coefficient where the summation of the coefficients is equal to 1, M_j is one chemical element from the periodic table, and j represents the index of that element ($j = 1...n$). It is due to the use of this superposition with constraints on coefficients that we name our method QCE.

⚡ **CellPress**

Matter
Article

In this study, we use the encoding $c(M_j) = q_j$, where q_j is a binary variable only accepting 0 and 1 as the values. Such variables are quite often realized as spins of a quantum annealer or binary decision variables in quantum-inspired optimizers. Several other candidate functions can also be used for the encoding scheme $c(\cdot)$ (refer to the methods section "Encoding schemes for QCE" for an in-depth analysis of alternative encoding schemes). Using the encoding $c(M_j) = q_j$ transforms Equation 3 as

$$\Phi_i(\sigma_i) = \sum_{j=1}^{n} q_j \cdot \varphi_i(\sigma_i = M_j) \qquad \text{(Equation 4)}$$

Substituting for Φ_i from Equation 4 in Equation 2 yields an expression with several multi-body interaction terms ($q_o q_1$, $q_0 q_1 q_2$, $q_0 q_1 q_3 q_4$, ..). We use term reduction as reported by Babbush et al.[40] to simplify the expression repeatedly until a QUBO expression is obtained:

$$P = \sum_{i,j=1}^{N'} A_{ij} q_i q_j \qquad \text{(Equation 5)}$$

where A_{ij} are QUBO coefficients that are a function of J_f, Π_f and penalties used for term reduction. q_i is a binary decision variable accepting only 0 or 1 as the value. N' is the total number of decision variables including the auxiliary variables used for term reduction.

The QUBO expression is then transferred to DA for efficient search and finding configurations that have the optimal property (minimum or maximum). Since any QUBO expression can be mapped to an Ising Hamiltonian, our proposed approach can be used by any Ising model solver such as a quantum annealer for optimizing materials within chemical space. This further motivated the term "QCE." The complete process is summarized in Figure 1.

Benchmarking our approach through exploration of quaternary chemical space (Cu-Ni-Ag-Pd)

To benchmark the performance of our proposed approach, we explored the quaternary chemical space spanned by Cu-Ni-Ag-Pd in a face-centered cubic (FCC) lattice due to their potential applications as fuel cell membranes[41] and oxygen reduction electrocatalysts.[42] Stability of materials for such applications is critical and is being extensively investigated.[41,43] Thus, finding stable alloys within this chemical space can be an exciting prospect[41,44] (Figure 2A). We use DFT for data generation and perform structure relaxation on randomly decorated FCC structures, followed by evaluation of the total energy of the systems. These total energies are then used to calculate mixing energies (ΔH_{mix}), which are used to train a CE model (refer to the sections "Data generation" and "Mixing energy (ΔH_{mix})" for more details) and use it a measure of alloy's stability against its single metal constituents. The model achieves a 10-fold cross-validation mean absolute error (MAE) of 8 meV/atom (Figure 2B; see methods section "CE training" for more details). We used CE with two-body and three-body interactions with cutoff radius of 12 Å as we found it to be most accurate in terms of cross-validation mean absolute error.

Using the scheme presented in the previous section, we prepared the QUBO representation of our CE model and transferred it to the DA for finding structures with minimum mixing energy (refer to the methods section "DA" for more details). To explore the potential of our approach, we sought to determine stable alloys within the Cu-Ni-Pd chemical subspace. We achieved this by restricting the possible values

CellPress
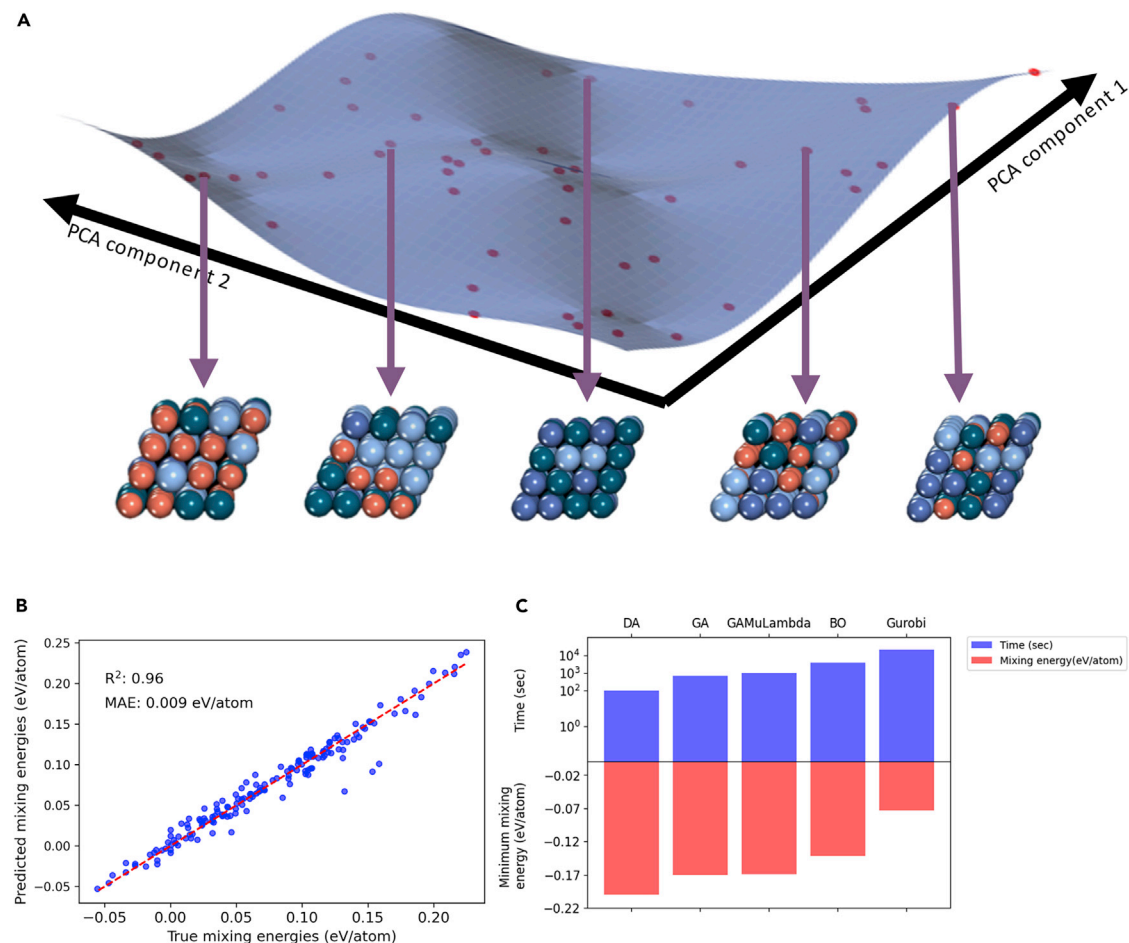
Figure 2. Chemical space exploration using proposed mapping

Exploring chemical space with random sampling often ends up with limited exploration. Accurate surrogate models and search algorithms can help us explore unsampled chemical territories.

(A) The mixing energy landscape in a 2D projection of the chemical space. Red dots correspond to the sampled points and each of the points in this 2D projection correspond to a chemical structure. The global minimum has not been sampled.

(B) CE predictive accuracy for quaternary alloy composed of Cu-Ni-Pd-Ag (our benchmark materials system).

(C) Performance of our QCE approach using DA against other widely used algorithms. We perform chemical ternary subspace search in Cu-Pd-Ni space. We observe significant temporal acceleration against genetic algorithms (GAs) and its variant MuPlusLambda in addition to bayesian optimization (BO) and a commercial optimization solver Gurobi. The ground states found by the different solvers vary with only DA providing the actual ground state configuration and composition. Refer to section ''methods'' on benchmark algorithms for details on implementation.

of the basis function Φ_i to only include relevant elements in the expansion of Equation 3 (refer to the methods section "Chemical subspace search" for more details). Upon performing the search using DA, we obtained equimolar ordered $Cu_{0.5}Pd_{0.5}$ alloy as the alloy with most negative mixing energy ($\Delta H_{mix} = -0.20$ eV/atom) in Cu-Ni-Pd space and, therefore, it is stable (Figure S2). This observation is independently supported by a previous report about equimolar FCC Cu-Pd alloy being the more stable.[44]

Furthermore, we compared the temporal and efficiency performance of our approach to other widely used search algorithms in chemistry and material science: genetic algorithms (GAs) and bayesian optimization (BO). We implement the GAs through distributed evolutionary algorithms in Python (DEAP) framework[45] and BO using scikit-optimize[46] (for exact implementation, please refer to our code).

 CellPress

Matter
Article

We find that our approach when used in combination with the DA significantly out-performs the alternatives in finding the minimum mixing energy structure (Figure 2C; logarithmic scale). We also observe that our approach results in better quality of global minima. Even though the energy difference between QCE-based predictions and best GA-based predictions is 0.03 eV/atom, the ground state structures found by them are significantly different ($Cu_{0.5}Pd_{0.5}$ and $Cu_{0.69}Pd_{0.31}$ respectively) indicating the importance of accurate search algorithms. In addition, when we compare the results of DA against BO, we observe much worse performance than DA as well as GA. The final compositions found by BO were much closer to the starting points, indicating that BO used in our comparisons is more effective in searching for local optimum than global optimum. All the tests were performed using a 20 core Intel Xeon 6148 CPU operating at 2.4 GHz. Detailed parameters for all the comparison algorithms are presented in the methodssection "Performance benchmark algorithms."

Finding stable and efficient OER materials

To demonstrate the generalizability of our approach, we showcase the discovery of acidic OER catalysts.[47,48] The development of OER catalysts has been the subject of significant research over the past few years.[5,43,49-53] For the alkaline medium, several stable and efficient OER catalysts have been proposed; however, only a few stable, efficient, and cost-effective OER catalysts have been reported in literature for operation in an acidic medium.[50,54]

High efficiency and high stability are two crucial requirements for a good OER catalyst. To develop a quantitative model for efficiency of the catalyst candidates, we built upon the d-band model by Hammer and Nørskov[55-58] and recent studies about its interplay with p-band centers.[59] We used materials and alloys constructed by substituting two different prototype structures: ZrO_2 ($P2_1/c$; monoclinic) and RuO_2 ($P4_2/mnm$; tetragonal) in our study. We generate slabs to model the catalytic activities for randomly generated structures (refer to methods section "Data generation"). After performing DFT calculations, we used the adsorption energies to determine the theoretical overpotentials (refer to Figure S4 for model of the slabs). We performed logistic regression on the differential improvement of overpotential; i.e., if overpotential of one material is smaller than the other (refer to methods section "Logistic regression analysis"; Figure 3A). We observe that the probability of material i having an overpotential smaller than materials j is given by the following expression:

$$Prob(\eta_i < \eta_j) = \frac{1}{1 + e^{\theta}}$$

(Equation 6)

$$where \ \theta = 0.078 \cdot \left(E_{p_i} - E_{p_j}\right) - 0.165 \cdot \left(E_{d_i} - E_{d_j}\right)$$

where η represents overpotential and E_p and E_d represent p-band center and d-band center, respectively.

To further establish the validity of this theoretical analysis, we further conduct several in-laboratory experiments. Using just the contributions due to band centers, we achieve a Pearson's correlation coefficient of 0.67 (p < 0.001) between experimental overpotentials and theoretical proxy. We also observe that, when combined with enthalpy of mixing (ΔH_{mix} per atom), we observe a significant improvement in predictive power using simple Ridge regression. Inclusion of mixing energy as a predictor significantly improves 10-fold cross-validation correlation from 0.67 to 0.81 (Figures 3B and 3C; Note S3). This role of mixing energy as a predictor can
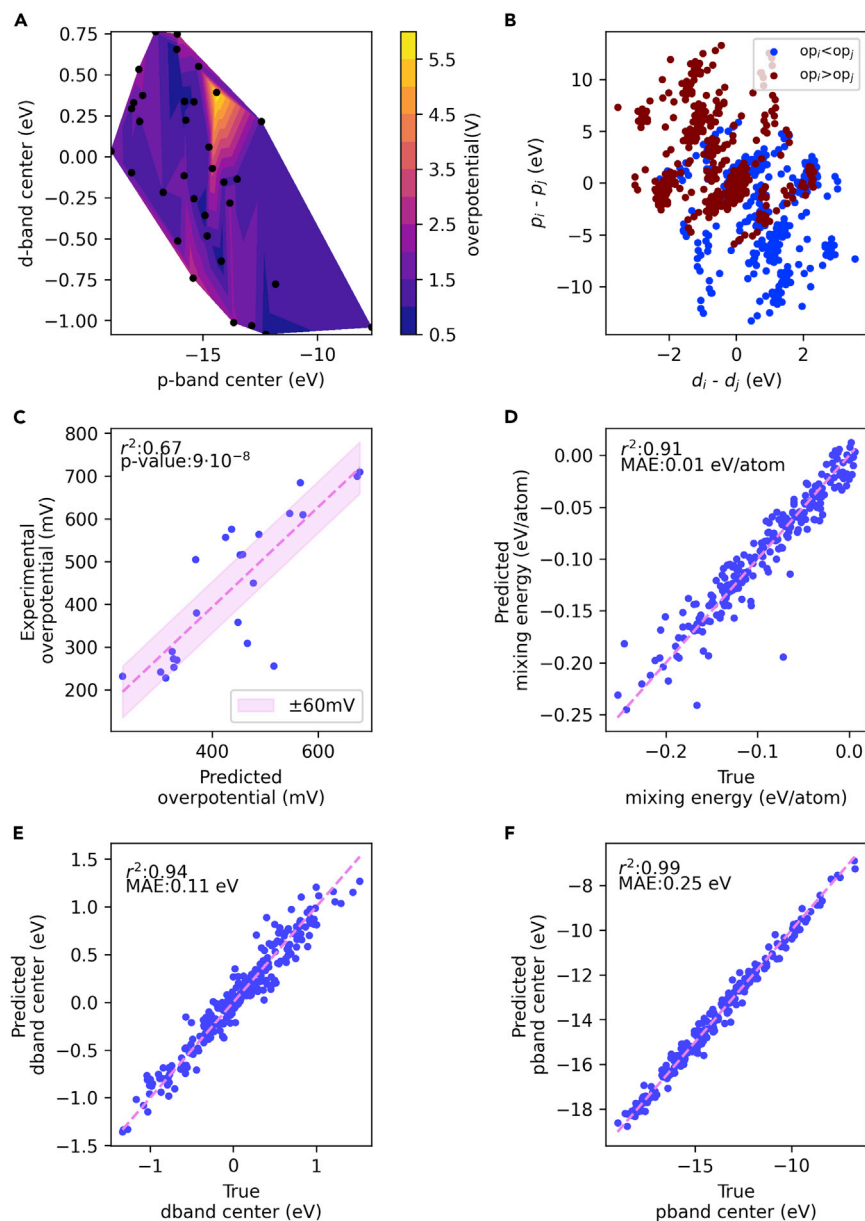
Figure 3. Development of an efficiency proxy for OER catalysts and training the CEs

(A) The relationship between electronic structure of the material and its efficiency expressed through overpotential. We trained a logistic regression-based classifier to assess whether one material has a larger overpotential than the other (0 if smaller and 1 if larger) and use it to search for more efficient materials.

(B) We further validate this hypothesis on overpotentials obtained through in-laboratory experiments as part of this study; when represented as band centers, we are able to cluster the differences with high accuracy.

(C) How the theoretically calculated d- and p-band centers correlate with experimental overpotentials. We use the exact coefficients obtained through logistic regression comparison classifier to perform this analysis.

(D–F) The performance of CE models used for exploration within this study for mixing energies.

(D) Predictions of the bulk structures for [Ru-Cr-Mn-Sb-Ti-V-W-Co]O_2.

(E) Performance of CE model in predicting d-band centers of the bulk structures for [Ru-Cr-Mn-Sb-Ti-V-W-Co]O_2.

(F) Performance of CE model in predicting p-band centers of the bulk structures for [Ru-Cr-Mn-Sb-Ti-V-W-Co]O_2.

be explained as stable catalysts are likely to catalyze the reaction consistently. The overall expression to predict overpotentials η is expressed as,

$$\eta_i = K(0.046E_p - 0.097E_d - \Delta H_{mix} + C) \qquad \text{(Equation 7)}$$

where E_p is p-band center, E_d is the d-band center, ΔH_{mix} is mixing energy in eV/atom, C is a constant, and K is just a multiplier. The values for the three properties are not on the same scale and that explains the large variation in the absolute value of coefficients. For exact values of K and C, please refer to Note S3. We also report all the collected experimental quantities for the candidates with measurable activity and acidic stability in Table S3 as a tabular database for future ML explorations and for reference. In addition, we also used mixing energy ΔH_{mix} to quantify stability of an alloy relative to its precursors (i.e., ease of synthesizability of the alloy).

Following the strategy for QCE, we trained CE models (Figure S5; methods section "CE training") and generated the QUBO representations for each of the three properties, ΔH_{mix} (H_E), p-band center (H_p), and d-band center (H_d), using QCE. These properties were obtained by first performing DFT geometry optimization on the initial decorated lattices followed by calculation of the converged electronic and thermodynamic properties. Performing cross-validation analysis to find the optimal cutoffs, we find that CE models with 4 and 8 Å cutoffs for two-body and three-body interaction terms lead to the best predictive power. Similarly, for predicting d-band centers, the highest predictive power is demonstrated by a CE with 12 and 6 Å cutoffs for two-body and three-body interactions. A CE model that incorporated just two-body interactions with a cutoff of 4 Å achieved the best predictive power. The accuracy and performance of each of these models on validation data are shown in Figures 3D–3F. We defined QUBO for efficiency as,

$$H_{eff} = 0.046E_p - 0.097E_d - \Delta H_{mix} \qquad \text{(Equation 8)}$$

Thus, the problem of finding an efficient and stable OER catalyst transforms into finding a state that minimizes both H_{eff} and H_{stable} where H_{stable} is the QUBO representation for mixing energies. We solve this problem by using a heuristic approach of optimizing the linear combination of the two QUBOs:

$$H_{mixed} = \lambda_1 H_{stable} + \lambda_2 H_{eff} \qquad \text{(Equation 9)}$$

where $\lambda_1, \lambda_2 \in [0, \infty)$ (refer to Figure S6 for the effect of parameters λ_1, λ_2). Transferring H_{mixed} represented as QUBO to DA and performing the optimization result in candidates that have promising stability as well as efficiency.

We searched for different chemical subspaces within the two prototype structures by varying the relative weight parameters λ_1, λ_2 and chemical subspace of interest (Figure S7) while adding constraints to ratios of different elements (refer to Figure 4 for a summary of candidates experimentally tested and Table S1 for a detailed list), whereas non-zero pairs lead to a balanced trade-off between stability and efficiency (Figure S6). We also compare this approach with a sequential search (search for stability followed by efficiency). We find that our heuristic approach outperforms a sequential search strategy (Note S7). In our searches, we focused on exploring ternary and quaternary chemical spaces. This choice was motivated by existing exploration of binary transition metal oxides in the literature[5,43] as well as effectiveness of the sol-gel method of synthesis for multi-metal oxide synthesis.

In the context of the presented QCE method for chemical space search, it is also worth noting the previous studies by Pedersen et al.[60] on usage of BO for catalyst search. Both the observations made by the authors of that study and our
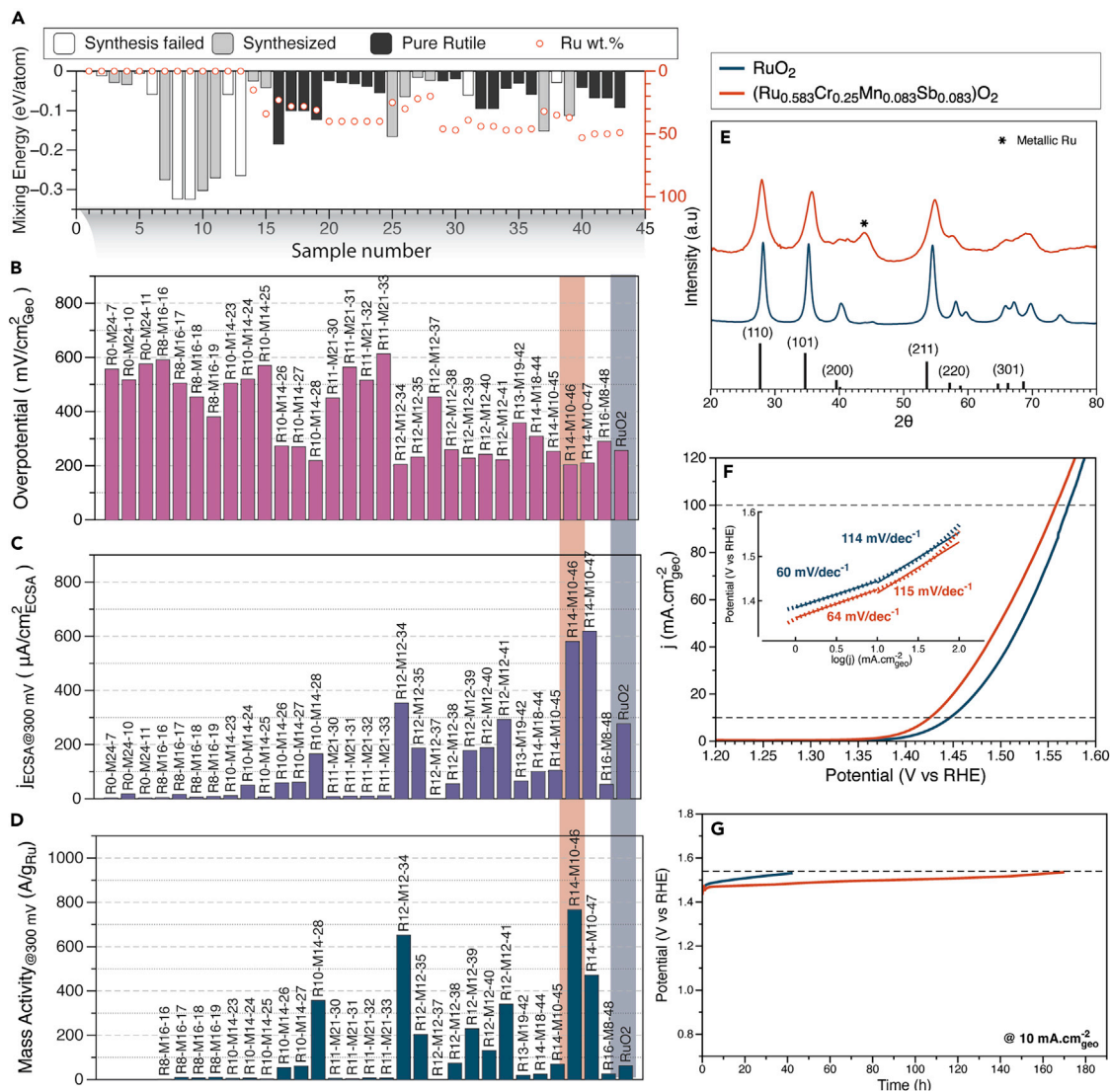
Figure 4. Experimental screening of electrocatalysts

(A) The mixing energy of all electrocatalyst candidates considered for experiments in this study. The candidates were classified based on the synthesis outcome: synthesis failed (the electrocatalyst was not produced), synthesized, and pure rutile phase.

(B) Overpotential screening of synthesized electrocatalysts.

(C) The intrinsic activity of electrocatalysts normalized by the electrochemical surface area.

(D) The mass activity of electrocatalysts normalized by the total mass of Ru.

(E and F) (E) XRD and (F) polarization curves (Tafel slope analysis in the inset) of the best electrocatalyst candidate R14-M10-41 $(Ru_{0.58}Cr_{0.25}Mn_{0.083}Sb_{0.083}O_2)$ and a baseline RuO_2 catalyst.

(G) Chronopotentiometry test of the electrocatalysts sprayed on carbon paper electrodes. In the inset is the accelerated test conducted on the electrocatalysts drop-casted on carbon paper. The electrocatalyst loading for all samples is 1 mg/cm². The electrolyte is 0.5 M H_2SO_4.

benchmarking experiments indicate that a BO-based search strategy is better suited to a local optimum search than a global optimum. So, if the question is to find a globally optimal material, QCE will outperform BO-based approaches. On the other hand, both BO and QCE with constraints can be used for local optimizations of materials within the chemical space. With QCE, we can constraint the elemental fractions as inequalities and perform local chemical space search.

Experimental verification

All of the 49 electrocatalyst candidates in Table S1 were synthesized using sol-gel synthesis followed by annealing in air for 2 h.[61] We observed that some compositions (eight compounds) were not successfully synthesized using the sol-gel method due to poor promotion of networks in the gel (Figure 4A). The crystal structure of the synthesized samples was screened using X-ray diffraction (XRD). XRD patterns were collected and classified into two groups: pure rutile phase (21 compounds) and multiple-phases groups (20 compounds). One XRD pattern is shown in Figure 4E for $Ru_{0.58}Cr_{0.25}Mn_{0.08}Sb_{0.08}O_2$ (R14-M10-46) showing characteristic peaks of a rutile structure similar to a baseline RuO_2 catalyst. The XRD peaks are broad, indicating that our synthesis approach produced nanocrystalline electrocatalysts. Further analysis of the structure for all electrocatalysts is provided in Table S2. High-resolution transmission electron microscopy (HR-TEM) and scanning transmission electron microscopy (STEM) are shown for three samples in Figure S8. The nanoparticles have an average particle size of ∼10 nm with a spherical shape suitable for electrocatalytic applications. The energy X-ray dispersive spectroscopy (EDS) elemental mapping shows a homogeneous distribution of elements in the three samples (Figure S9). The EDS elemental mapping of $Ru_{0.58}Cr_{0.25}Mn_{0.08}Sb_{0.08}O_2$ (R14-M10-46) matches within 5% error with the nominal composition of the compound (Ru, 59 ± 5.9 atom %; Cr, 20 ± 1.0 atom %; Mn, 9 ± 0.6 atom %; Sb, 13 ± 3.4 atom % of the total metal amount). The electron diffraction rings of the three samples confirm the formation of a strained rutile structure (Figure S10).

The electrocatalysts were then drop-casted on carbon paper to screen the electrochemical performance. The overpotential of the electrocatalysts was measured in a three-electrode cell using 0.5 M H_2SO_4 (Figure 4B; Table S3). The experimental overpotentials matched well with the trend of predicted activity (Figure 3C; Note S3). We observe a coefficient of determination of 0.71 between our theoretically derived quantum mechanical proxy and in-laboratory experimental overpotential of catalyst candidates ($p < 0.001$). We used the structures as obtained by optimization of Equation 9 to model every chemical composition. Furthermore, to compare the intrinsic activity of the electrocatalysts, we decoupled the morphology effect from the activity by normalizing the current density by the active electrochemical surface area overpotential instead of the geometric area (Figures 4C and S11). We then calculated the mass activity of the electrocatalysts normalized by the Ru amount in the electrocatalyst (Figure 4D). Taking into consideration both measures, we identified $Ru_{0.58}Cr_{0.25}Mn_{0.09}Sb_{0.08}O_2$ as the most promising candidate with the highest mass activity 381 A/g_{Ru} (about eight times higher than RuO_2) and a much lower overpotential increase rate of 2 mV h^{-1}, 10 times slower than RuO_2 (inset in Figure 4G; Table S3).[62] To better assess the stability of the electrocatalyst, we prepared it by spraying the electrocatalyst on carbon paper instead of drop-casting, the technique we used for screening purposes, to ensure a higher penetration of the particles through the hydrophilic carbon paper yielding in higher surface coverage and better mechanical attachment to the carbon fibers. We maintained the loading of the electrocatalyst between both preparation techniques at 1 mg/cm^2. Our candidate maintained an overpotential of less than 300 mV for 180 h at a low overpotential increase rate of 2 mV/h, 10 times lower than RuO_2 and any previous reports of rutile structure-based catalysts.[43] Finally, we also search existing databases (OQMD, AFLOW, Materials Project, OCP, ICSD) and literature for similar alloys and we were unable to find even a similar oxide compound with Ru, Cr, Mn and Sb present together. Our QCE method was therefore able to effectively search chemical space, identify a new promising family of multi-metal oxides for exploration, and discover a highly efficient and stable OER catalyst.

Matter
Article

CellPress

We also compared the results with a random sampling of chemical composition strategy. We observed that five out of eight of our predictions demonstrated an overpotential of less than 300 mV, and three of them demonstrated an exceptional stability of less than 10 mV/h overpotential degradation (Table S3). If we had to randomly sample the chemical space to find at least one of these three compositions, we would need to perform at least ~766 experiments in the quaternary chemical space of just a single chemical subspace (see Note S8 for stoichiometric space size), indicating at least 95× improvement over a random chemical space search strategy purely based on experiments.

DISCUSSION

Origins of the catalyst stability and efficiency

To better understand the cause of higher activity and stability of our top catalyst candidate, $Ru_{0.58}Cr_{0.25}Mn_{0.09}Sb_{0.08}O_2$ (henceforth referred to as catalyst $RuCrSbMnO_2$), we performed detailed DFT calculations and analysis. We used the crystal structure for each candidate, as obtained by minimizing the joint Hamiltonian in Equation 9, for performing the following analysis (Figures S12 and S13 for crystal structure of $RuCrMnSbO_2$ and its XRD comparison to experimental structure). Bader charge analysis showed that the average partial charge on Ru increased from **1.73|e|** in pure RuO_2 to **1.82|e|** in $RuCrMnSbO_2$. Ru with a higher partial charge indicates improved ability of the catalyst to oxidize water to oxygen (i.e., OER). Additionally, to explore the origin of the stability of the catalyst candidates, we further analyzed the density of states (DOS). As shown in Figures 5A and 5B), incorporation of Cr, Mn, and Sb alter the DOS of RuO_2, causing occupation at Fermi level to decrease from 38 states/spin · cell to 18 states/spin · cell. This decrease in DOS at fermi energy indicates stronger bonding between metal atoms, leading to stabilization of our solid solution[43,63] (see Figure S14 for a comparison study that considers only Cr and Mn). Table 1 summarizes our observations against previously reported $Ru_{0.4}Cr_{0.6}O_2$ and RuO_2.[43] We also observe that entropic contributions further stabilize the predicted composition $RuCrMnSbO_2$ compared with previously reported RuO_2 and $Ru_{0.4}Cr_{0.6}O_2$. These observations align with our observed experimental measurements of 180-h stability for $RuCrMnSbO_2$ compared with unstable $RuCrO_2$ and 40-h stability of pure RuO_2 (catalyst ID R8-M16-16 and RuO_2 for detailed experimental results on stability and activity in Tables S1–S3).

At the same time, we calculated free-energy profiles (ΔG) of OER to compare the activities of $RuCrMnSbO_2$ with RuO_2 (refer to methods section "Data generation" for details and Notes S5 and S6). As can be seen from Figure 5 (C and D), the formation of OOH was found to be the rate-determining step. For $RuCrMnSbO_2$, the Bader charge was found to be 1.92 eV, which is smaller than the Bader charge corresponding to RuO_2 (2.02 eV) and consistent with the experimental observation of smaller overpotentials. This observation can be explained by the finding that the d-band surface DOS is higher for $RuCrMnSbO_2$ (7.52 states/spin · cell) compared with RuO_2 (5.30 states/spin · cell), leading to the lower overpotential and lower reaction energy barrier to the formation of adsorbed OOH radical. Presence of larger number of states enables easier electron transfer and, therefore, facilitates formation of intermediates (*O, *OH, *OOH).[64]

Conclusions

In this study, we reported a new approach for materials discovery that maps the chemical space search problem to one of finding the ground state of the Ising Hamiltonian. This enables us to use a quantum-inspired computing framework to find materials with optimal properties in an accelerated and efficient fashion, orders of magnitude faster than the widely used alternatives, such as GAs and BO. Our efforts led us to develop an improved efficiency proxy and discover a stable and efficient
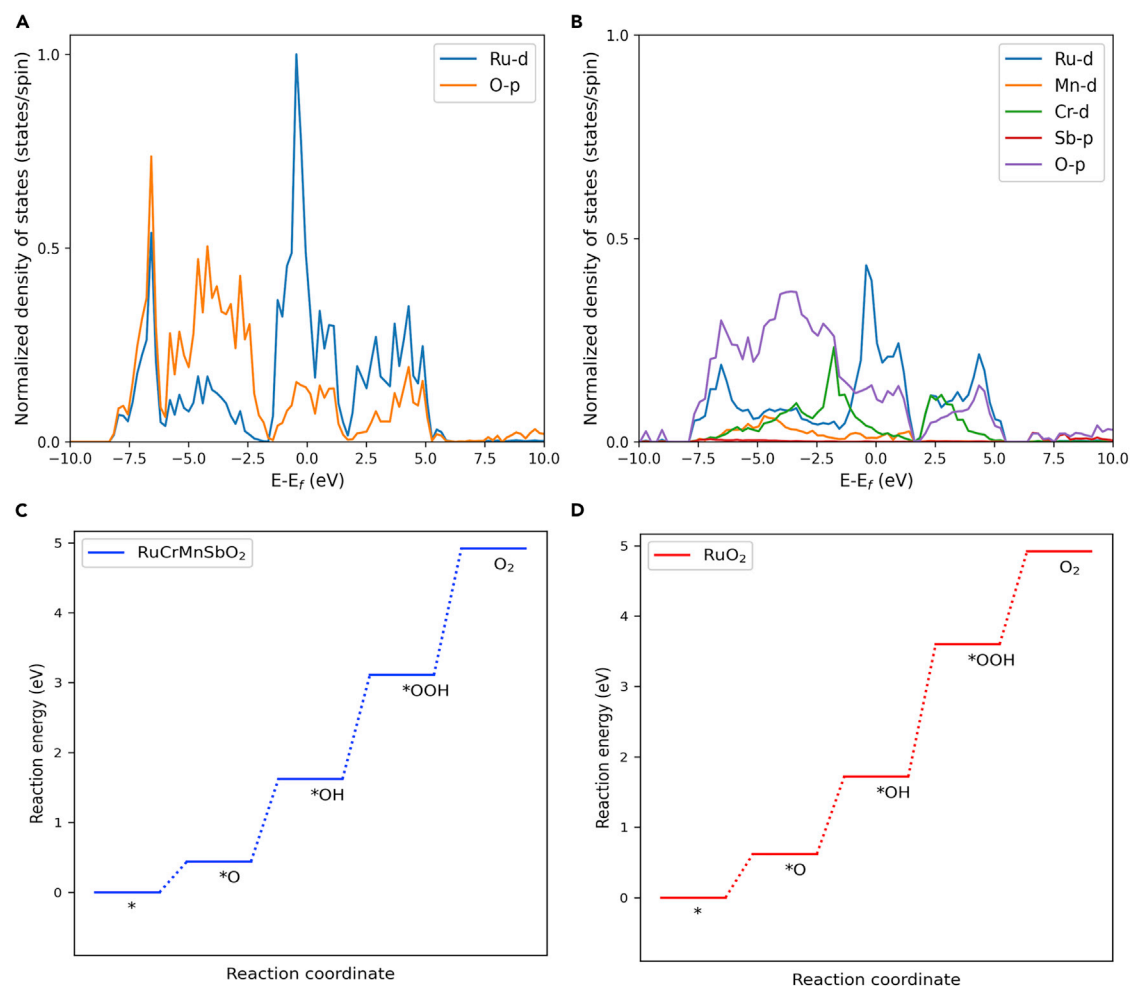
Figure 5. Post hoc DFT analysis of the best candidates

(A) Bulk DOS decomposed into elemental contributions and normalized to one for all the constituent elements for RuO_2.

(B) Elemental decomposed DOS for bulk $RuCrMnSbO_2$ using the same normalization scale. We observe that the DOS for RuO_2 at fermi level is 38 states/(eV · spin) larger than 18 states/(eV· spin) in $RuCrMnSbO_2$, which is an indicator of better chemical bonding.[63]

(C) Free-energy diagram for OER for RuO_2 catalyst.

(D) Free energy diagram for OER with $RuCrMnSbO_2$ catalyst. In both cases, *OOH formation is the rate-determining step (RDS) with $\eta_{RuO_2} > \eta_{RuCrMnSbO_2}$ where η represents overpotential.

OER catalyst $Ru_{0.58}Cr_{0.25}Mn_{0.09}Sb_{0.08}O_2$. Post hoc DFT analysis further explains the electronic origins of the stability and efficiency of the catalysts.

However, we should also take note of one of the limitations of the current study: restriction of one lattice across the chemical space, which is not what is always desired in materials discovery pipelines. Nevertheless, this can be handled by using extended CE mapping as proposed by Koretaka Yuge.[65] We plan to incorporate this as part of our future work.

EXPERIMENTAL PROCEDURES

Resource availability

Lead contact
The lead contact for this paper is Edward H. Sargent (ted.sargent@utoronto.ca).

CellPress

Table 1. Comparison of different stability contributing factors for RuO_2, $Ru_{0.4}Cr_{0.6}O_2$, and $RuCrMnSbO_2$

Compound	ΔH_{mix} (eV/atom)	Bader charge on Ru	DOS at E_{fermi} (states/spin · cell)	Entropy contribution at 550 °C (eV/atom)
$RuCrMnSbO_2$	−0.08	1.82	18	−0.078
$RuCrO_2$	−0.05	1.92	19	−0.048
RuO_2	0.0	1.73	38	0.000

Materials availability

This study did not generate new unique reagents.

Data and code availability

All the code and data supporting this study are available at a public Github repository: https://github.com/hitarth64/quantum-inspired-cluster-expansion. The repository contains all the code required to run the searches and data used for bulk periodic systems within the study.

All the slab calculation data are available at: https://github.com/hitarth64/Mixed MetalOxides.

Methods

DA

Fujitsu's DA is designed to efficiently solve combinatorial optimization problems[27] formulated as fully connected Ising problems expressed in QUBO form. In the most general case, a QUBO can be represented as $F(q_0, q_1, \ldots, q_n) = \sum_{ij} a_{ij} q_i q_j$, where q_i ($i = 1 \ldots n$) are binary variables.

In this work, we used a third-generation DA, which can handle up to 100,000 binary decision variables. Given a QUBO expression, the DA finds the assignment of binary variables (referred by $q_0, q_1, \ldots$) such that the expression value is minimized. All experiments were conducted on the DA environment prepared for research use. More details on exact algorithms and configuration of DA can be found at: https://www.fujitsu.com/jp/documents/digitalannealer/researcharticles/DA_WP_EN_20210922.pdf.

Data generation

We use RuO_2 (Materials Project[66]: mp-825) and ZrO_2 (Materials Project: mp-2858) as the prototype structures and generated 72 and 96 atom supercells, respectively, for training the CE models. Then, 120 randomly substituted alloy structures were generated for each of the chemical spaces spanned by Ru-Ti-W-Sb-Cr-Mn-V-Co and Ru-Zr-Hf-Y-V-Co-Fe-Ce. We further randomly selected 34 structures and generated surfaces with 110 orientations for the calculation of adsorption energies with vacuum spacing of 10 Å on both sides. We chose 110 orientations since we found it to be most stable with respect to surface energy (refer to Note S6). The slab models were composed of 144 atoms (48 metal atoms and 96 oxygen atoms) repeated in four layers besides the adsorbates (O, OH, and OOH). DFT calculations were performed in Vienna ab initio simulation package (VASP) for the bulk and surface structures using Perdew-Burke-Ernzerhof[67] (PBE) exchange-correlation functional augmented with Hubbard coulomb interaction potential (U) corrections for d-electrons taken from Materials Project.[66] Valance electrons were described with a 520-eV plane-wave basis set and 0.05 eV Gaussian smearing of the electronic density. All the bulk geometries were optimized with the energy convergence criterion of 10^{-4} eV and force convergence of 0.03 eV/Å. Core electrons were described using the projector augmented wave (PAW) method. All the calculations were spin polarized and reciprocal space was simulated using a 3 × 2 × 1 k-points mesh

CellPress

Matter
Article

centered at gamma. Refer to Note S2 for a detailed evaluation of the computational costs associated with a single calculation.

For Cu-Pd-Ni-Ag chemical space benchmark, we used Cu-FCC 64 atoms supercell as the prototype structure, and 120 randomly decorated structures were generated. DFT calculations were performed in VASP for the bulk using Perdew-Burke-Ernzerhof[67] (PBE) exchange-correlation functional. Valance electrons were described with a 520-eV plane-wave basis set and 0.05 eV Gaussian smearing of the electronic density. All the geometries were optimized with the energy convergence criterion of 10^{-4} eV and force convergence of 10^{-3} eV/A. Core electrons were described using the PAW method.

To perform *post hoc* DFT analysis of the RuO_2 and $RuCrMnSbO_2$, we generated surfaces with orientations [001, 100, 101, 110] and choose 110 as the orientation to perform adsorption energy calculations due to lower energy (Note S5). The *post hoc* DFT analysis was done on a k-points grid 3 × 2 × 1 with 520 eV as the energy cutoff for the PAW pseudopotentials and strongly constrained and appropriately normed (SCAN) exchange-correlation functional was used with the Hubbard-U correction. The rest of the parameters stayed the same as in the preceding paragraph.

Mixing energy (ΔH_{mix})
We define mixing energy or enthalpy of mixing ΔH_{mix} as excess energy with respect to the single metal precursors. For metal alloys it assumes the form

$$\Delta H_{mix}\left(A_x B_y C_z D_w\right) = E\left(A_x B_y C_z D_w\right) - \frac{x \cdot E(A_u) + y \cdot E(B_u) + z \cdot E(C_u) + w \cdot E(D_w)}{u}$$

where $u = x + y + z + w$ and $E(\cdot)$ represents total energy of the concerned phase.

Similarly, for mixed metal oxides, it assumes the form

$$\begin{aligned}\Delta H_{mix}\left(A_x B_y C_z D_w O_v\right) &= E\left(A_x B_y C_z D_w O_v\right) \\ &- \frac{x \cdot E(A_u O_v) + y \cdot E(B_u O_v) + z \cdot E(C_u O_v) + w \cdot E(D_w O_v)}{u}\end{aligned}$$

where $u = x + y + z + w$.

CE training
We used integrated cluster expansion toolkit (ICET) to train CE models.[37,68] The scripts and codes are available at https://github.com/hitarth64/quantum-inspired-cluster-expansion. We tested different cluster generation schemes by tuning the kind of interactions and cutoff for each of the interactions (see Figure S5 for a comparison plot). Parameters that lead to the lowest cross-validation error were chosen for analysis.

Encoding schemes for QCE
Several candidate functions can be used for the encoding scheme $C(\cdot)$. Two natural choices are as follows:

- Encoding 1:

$$\Phi_i(\sigma_i) = \sum_{j=1}^{n} q_j \cdot \varphi_i\left(\sigma_i = M_j\right)$$

CellPress

where q_j are binary decision variables and the one-hot constraint of Equation 3 is then enforced as a penalty:

$$P_i(\sigma_i) = \left(\sum_{i=1}^{n} q_i - 1 \right)^2$$

- Encoding 2:

$$\Phi_i(\sigma_i) = \sum_{j=1}^{n} f_j(q_1, q_2, \ldots q_k) \cdot \varphi_i(\sigma_i = M_j)$$

where q_j are binary decision variables, $k = \text{ceil}(\log_2 n)$ where n is total number of element types. Functions $f_j(\cdot)$'s are defined such that only one $f_j(\cdot)$ is non-zero and others are zero for any $\vec{q} \in \{0,1\}^k$ and each $f_j(\cdot)$ is one at leas for one $\vec{q} \in \{0,1\}^k$. Here are the steps to construct such f_j. First, for each possible bit string in the space $\{0,1\}^k$, construct a polynomial that takes one only for the bit string and zero for other bit strings. Next, determine a surjection from the bit strings to element indices $\{1 \ldots n\}$. Finally, define f_j as the sum of the polynomials correspond to bit strings that mapped to the element j in the previously defined surjection. Such an encoding scheme trivially enforces the one-hot constraint of Equation 3 and therefore, we do not need to add it as a penalty. For a three elements system example, the bit strings and the corresponding polynomials are $\{0,0\}$ and $(1 - q_1)(1 - q_2)$, $\{0,1\}$ and $(1 - q_1)q_2$, $\{1,0\}$ and $q_1(1 - q_2)$, and $\{1,1\}$ and $q_1 q_2$. An instance of surjection is $\{0,0\} \mapsto 1, \{0,1\} \mapsto 2, \{1,0\} \mapsto 3, \{1,1\} \mapsto 3$. In this case, $f_1 = (1 - q_1)(1 - q_2)$, $f_2 = (1 - q_1)q_2$, $f_3 = q_1(1 - q_2) + q_1 q_2 = q_1$.

Performance benchmark algorithms

We performed comparison against four heuristic search algorithms that are widely used in chemistry and material science. Their implementation details are as follows:

- GA: GA is implemented using the DEAP framework.[45] We use eaSimple algorithm with 300 generations and a population size of 300 to run and perform the searches. We use crossover and mutation probabilities of 0.3 and 0.7.
- GAMuPlusLambda: this search method uses $(\mu + \lambda)$ evolutionary algorithm to perform the chemical space search using eaMuPlusLambda implementation as provided in DEAP. We use 300 generations and a population size of 300 with crossover and mutation probabilities the same as above. Corresponding μ and λ parameters that yielded the optimal solution were found to be 300 and 400.
- BO: we conducted BO-based searches to search and optimize the alloy combinations using scikit-optimize.[46] We specifically used Gaussian processes combined with a hybrid acquisition function that randomly chooses either lower confidence bound (LCB), expected improvement (EI), or probability of improvement (PI) at every iteration.
- Gurobi: we used commercial Gurobi 9.5.2 solver[69] and solved the chemical space optimization as a quadratic integer program. Gurobi is available free of charge for academic purposes.

The exact values are tabulated in Table 2.

Chemical subspace search

For performing QCE, we know from Equation 3 that we rewrite the CE formulation as

Table 2. Parameters of the different search algorithms used within the study (empty spaces correspond to absence of corresponding parameter in an algorithm)

Method	Global optimal solution (eV/atom)	Ground state	Time (s)	Generation	Population size	BO iterations	Iteration of saturation	Parameters
eaSimple	−0.181	Cu0.69Pd0.31	604	300	300		300	
DA	−0.200432	Cu0.5Pd0.5	80					
eaMuPlusLambda	−0.169	Cu0.65Pd0.35	1021	300	300		277	mu = 300, lambda_ = 400
Bayesian optimization	−0.1421	Cu0.7Ni0.04Pd0.26	3600			528	222	
Gurobi	−0.0742		20774					

$$\Phi_i(\sigma_i) = \sum_{j=1}^{n} C(M_j) \cdot \varphi_i(\sigma_i = M_j)$$

such that M_j, $j = 1 \ldots n$ represent the set of elements being considered for the site i and

$$C(M_j) \in \{0, 1\} \; \forall \; j$$

$$\sum_{j=1}^{n} C(M_j) = 1$$

In order to restrict the sampling to a set of elements, we limit the summation to set of elements of interest to us. If one wants to avoid element M_s, one can rewrite the summation as,
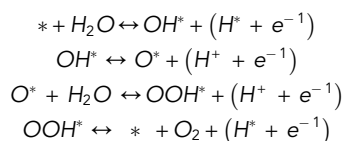
$$\Phi_i(\sigma_i) = \sum_{j=1, j \neq s}^{n} C(M_j) \cdot \varphi_i(\sigma_i = M_j)$$

Such that $C(M_j) \in \{0, 1\} \; \forall \; j$

$$\sum_{j=1}^{n} C(M_j) = 1$$

OER mechanism

OER in acidic and neutral medium is a four-step reaction with the following reaction mechanism[5,43,50]:

$$* + H_2O \leftrightarrow OH^* + (H^* + e^{-1})$$
$$OH^* \leftrightarrow O^* + (H^+ + e^{-1})$$
$$O^* + H_2O \leftrightarrow OOH^* + (H^+ + e^{-1})$$
$$OOH^* \leftrightarrow * + O_2 + (H^* + e^{-1})$$

where $*$ denotes the species adsorbed at the catalyst surface.

The theoretical overpotential (η_{OER}) is thus defined as

$$\eta_{OER} = \max \frac{(\Delta G_7, \Delta G_8, \Delta G_9, \Delta G_{10})}{e} - 1.23 \; V$$
$$= \frac{\max(\Delta G_{OH^*}, \Delta G_{O^*} - \Delta G_{OH^*}, \Delta G_{OOH^*} - \Delta G_{O^*}, 4.92 - \Delta G_{OOH^*})}{e} - 1.23 \; V$$

Calculation of η_{OER}, thus, requires values of adsorption energies for reaction intermediates O, OH, and OOH. These DFT energy calculations are computationally expensive. Usually, scaling relationships are used to reduce the number of calculations needed.[47] However, scaling relationships break down in the case of alloys. Therefore, here, we perform explicit DFT calculations for all three adsorbate structures, *O, *OH, and *OOH, along with bare surface to calculate the adsorption

energies. These adsorption energies along with zero point energies and entropic corrections are then used to calculate ΔG_{OH^*}, ΔG_{O^*}, and ΔG_{OOH^*} as

$$\Delta G_{O^*} = E_{DFT}(O^*) - E_{DFT}(*) - E_{DFT}(O) - E_{ZPE}(O) + T\Delta S(O)$$
$$\Delta G_{OH^*} = E_{DFT}(OH^*) - E_{DFT}(*) - E_{DFT}(OH) - E_{ZPE}(OH) + T\Delta S(OH)$$
$$\Delta G_{OOH^*} = E_{DFT}(OOH^*) - E_{DFT}(*) - E_{DFT}(OOH) - E_{ZPE}(OOH) + T\Delta S(OOH)$$

Furthermore, to overcome the limitation of traditional GGA-based calculations for O_2 molecule, its free energy is calculated as

$$G(O_2) = 4.92 + 2G(H_2O) - 2G(H_2) \ (in \ eV)$$

Calculation of band centers

D-band model relates the surface reactivity with the shifts in the d-band center of the catalyst where the d-band center is a single state with energy ϵ_d that approximates the interaction of participating bands of d-states. In particular, we calculated d-band centers and p-band centers using the first moments as

$$\epsilon_{M-d} = \frac{\int_{-\infty}^{\infty} ED_{M-d}(E - E_F) \, dE}{\int_{-\infty}^{\infty} D_{M-d}(E - E_F) \, dE} \qquad \text{(Equation 10)}$$

$$\epsilon_{M-p} = \frac{\int_{-\infty}^{\infty} ED_{M-p}(E - E_F) \, dE}{\int_{-\infty}^{\infty} D_{M-p}(E - E_F) \, dE} \qquad \text{(Equation 11)}$$

where M is the corresponding element and D_{M-y} represents partial DOS of orbital y of element M in the system.

Logistic regression analysis

We used logistic regression, as implemented in scikit-learn, to investigate the relationship between band centers and overpotentials of the materials. We first calculated theoretical overpotentials (section "OER mechanism") of 34 randomly chosen candidate materials from the two chemical families under consideration (section "Data generation"). We trained the classifier to distinguish the differential improvement between two catalysts; i.e., trained to predict whether $\eta_i < \eta_j$ (overpotential of material i is less than that of material j). In addition, refer to Figure S3 to see the variation in intermediate adsorption energies as a function of band centers.

Materials

Metal precursors including ruthenium chloride hydrate ($RuCl_3 \cdot xH_2O$), chromium(iii) chloride anhydrous, 99.99% trace metals basis ($CrCl_2$), manganese chloride ($MnCl_2$), tungsten (VI) chloride (WCl_6), titanium diisopropoxide bis(acetylacetonate), 75 wt % in isopropanol, vanadium(iii) chloride (VCl3), and propylene oxide ($\geq$99.5% GC) were all purchased from Sigma-Aldrich. Nafion (5 wt % in a mixture of lower aliphatic alcohols and water) and AvCarb MGL190 were used for electrode preparation. All chemicals were used without any further purification.

Experimental synthesis

The mixed metal oxides were synthesized using a modified sol-gel procedure[61] by completely dissolving a total amount of 2.7 mmol of the metal precursor mixture in 3.5 mL of anhydrous ethanol. The solution was vortexed for 5 min and sonicated in a water bath for 1 h until it was clear. Then, it was chilled in a refrigerator for 2 h to prevent any undesired hydrolysis and condensation, which may affect the gelation process. Afterward, a magnetic stirrer was used to mix the solution vigorously while 2 mL of propylene oxide was added dropwise to the mixture. The solution was aged for 1 day to promote gel formation and then washed with acetone; the process was repeated for 5 days before drying the gel in a vacuum oven for 1 day. The sol-gel

process produces amorphous oxides; therefore, to produce a rutile crystal structure, the dried powder was annealed at 400°C for 2 h.

For fast electrochemical purposes, the working electrode was prepared on 0.5 × 0.5-cm untreated carbon paper (AvCarb MGL190) by drop-casting. First, a catalyst ink was prepared by mixing 10 mg of the catalyst in 1 mL of a mixture of water and ethanol (4:1, v/v). Then, the ink was sonicated in an ice bath for 1 h. Finally, a 25-μL drop of the ink was deposited on the carbon paper and allowed to dry in the air. For final electrochemical testing, the working electrode was prepared by spraying the electrocatalyst using N_2 on 0.5 × 0.5-cm untreated carbon paper. The ink was prepared by mixing 10 mg of the catalyst in 1 mL of isopropanol. Then, the ink solution was sonicated in an ice bath for 1 h before spraying it on the carbon paper on the hot plate at 90°C.

Electrochemical testing
Electrochemical testing was conducted in a three-electrode setup using a Hg/Hg_2SO_4 as the reference electrode and graphite rod as the counter electrode. The OER activity was evaluated by running linear sweep voltammetry (LSV) with a rate of 5 mV/s. The stability of the catalyst was evaluated by conducting chronopotentiometry at 10 mA/cm^2.

All potentials were iR-corrected by measuring the solution resistance from electrochemical impedance spectroscopy (EIS) with a bias of 1.53 V vs. reversible hydrogen electrode (RHE) in the frequency range from 100 kHz to 10 MHz and an amplitude of 5 mV. All the potentials in this study were reported with respect to an RHE using the following relationship:

$$E_{RHE} = E_{Hg/Hg_2SO_4} + 0.640 + 0.0591 \times pH$$

Structure analysis
The crystal structure of catalysts was determined using X-ray diffraction (XRD). A Miniflex 600 (Rigaku, Japan) equipped with D/tex Ultra silicon trip detector and Cu Kα radiation (λ = 1.5418 Å) was used. Powders were prepared by mixing with acetone and then dropping a small drop of the mixture to fill a 4-mm-diameter by 100-μm-deep groove in a single crystal silicon holder (zero-background). The angle was varied between 20° and 80° with a step size of 0.005° and a scan rate of 1°/min.

To evaluate the nanocrystalline size and macrostrain of the electrocatalysts, we used Scherrer's equation and microstrain equation:

$$D = \frac{K\lambda}{FWHM\cos\theta}, \text{Scherrer's equation}$$
$$\varepsilon = \frac{FWHM}{4\tan\theta}, \ microstrain$$

D is the mean crystallite size, λ is 0.154 nm for Cu X-ray source, K is shape factor and has a typical value between 0.9 and 1. The full-width half-maximum (FWHM) of the peaks were measured by fitting to Gaussian distribution and then calculated from the standard deviation (σ) using the following relation:

$$FWHM = 2\sqrt{2.ln2} \approx 2.355\ \sigma$$

Electron microscopy
The structural characterization and elemental mapping of the catalysts were done using high-resolution scanning electron microscopy (HRSEM) and TEM. The experiments were conducted in a Hitachi HF3300 equipped with a cold field emission

electron gun using an accelerating voltage of 300 kV. An EDS detector was used in STEM mode to analyze and quantify the composition of the nanoparticles. Also, a secondary electron (SE) detector was used to collect HRSEM images of the nanoparticles. Powder samples were prepared in ethanol and sonicated for 10 min before drop-casting a 1- to 2-μL drop on a 400-mesh copper grid and drying overnight.

SUPPLEMENTAL INFORMATION

Supplemental information can be found online at https://doi.org/10.1016/j.matt.2022.11.031.

AUTHOR CONTRIBUTIONS

Conceptualization, A.A.G. and E.H.S.; methodology, H.C., J.A., D.M., H.M., M.S., Z.Y., and Z.W.; investigation, H.C. and J.A.; software, H.C. and H.M.; writing – original draft, H.C. and J.A.; writing – review & editing, E.H.S., A.A.G., and B.R.S.; funding acquisition, E.H.S. and Z.W.; resources, E.H.S.; supervision, E.H.S. and A.A.G.

DECLARATION OF INTERESTS

The authors declare no competing interests.

REFERENCES

1. Choudhary, K., Bercx, M., Jiang, J., Pachter, R., Lamoen, D., and Tavazza, F. (2019). Accelerated discovery of efficient solar cell materials using quantum and machine-learning methods. Chem. Mater. *31*, 5900–5908. https://doi.org/10.1021/ACS.CHEMMATER.9B02166.

2. Saidi, W.A., Shadid, W., and Veser, G. (2021). Optimization of high-entropy alloy catalyst for ammonia decomposition and ammonia synthesis. J. Phys. Chem. Lett. *12*, 5185–5192. https://doi.org/10.1021/ACS.JPCLETT.1C01242.

3. Kirman, J., Johnston, A., Kuntz, D.A., Askerka, M., Gao, Y., Todorović, P., Ma, D., Privé, G.G., and Sargent, E.H. (2020). Machine-learning-accelerated perovskite crystallization. Matter *2*, 938–947. https://doi.org/10.1016/J.MATT.2020.02.012.

4. Tao, Q., Xu, P., Li, M., and Lu, W. (2021). Machine learning for perovskite materials design and discovery. npj Comput. Mater. *7*, 23–18. https://doi.org/10.1038/s41524-021-00495-8.

5. Back, S., Tran, K., and Ulissi, Z.W. (2020). Discovery of acid-stable oxygen evolution catalysts: high-throughput computational screening of equimolar bimetallic oxides. ACS Appl. Mater. Interfaces *12*, 38256–38265. https://doi.org/10.1021/acsami.0c11821.

6. Jain, A., Voznyy, O., and Sargent, E.H. (2017). High-throughput screening of lead-free perovskite-like materials for optoelectronic applications. J. Phys. Chem. C *121*, 7183–7187. https://doi.org/10.1021/ACS.JPCC.7B02221.

7. Ren, Z., Tian, S.I.P., Noh, J., Oviedo, F., Xing, G., Li, J., Liang, Q., Zhu, R., Aberle, A.G., Sun, S., et al. (2022). An invertible crystallographic representation for general inverse design of inorganic crystals with targeted properties. Matter *5*, 314–335. https://doi.org/10.1016/J.MATT.2021.11.032.

8. Davies, D.W., Butler, K.T., Jackson, A.J., Morris, A., Frost, J.M., Skelton, J.M., and Walsh, A. (2016). Computational screening of all stoichiometric inorganic materials. Chem *1*, 617–627. https://doi.org/10.1016/j.chempr.2016.09.010.

9. Xie, T., and Grossman, J.C. (2018). Crystal graph convolutional neural networks for an accurate and interpretable prediction of material properties. Phys. Rev. Lett. *120*, 145301. https://doi.org/10.1103/PhysRevLett.120.145301.

10. Chen, C., Ye, W., Zuo, Y., Zheng, C., and Ong, S.P. (2019). Graph networks as a universal machine learning framework for molecules and crystals. Chem. Mater. *31*, 3564–3572. https://doi.org/10.1021/acs.chemmater.9b01294.

11. Park, C.W., and Wolverton, C. (2020). Developing an improved crystal graph convolutional neural network framework for accelerated materials discovery. Phys. Rev. Mater. *4*, 063801. https://doi.org/10.1103/physrevmaterials.4.063801.

12. Isayev, O., Oses, C., Toher, C., Gossett, E., Curtarolo, S., and Tropsha, A. (2017). Universal fragment descriptors for predicting properties of inorganic crystals. Nat. Commun. *8*, 15679. https://doi.org/10.1038/ncomms15679.

13. Rosen, A.S., Iyer, S.M., Ray, D., Yao, Z., Aspuru-Guzik, A., Gagliardi, L., Notestein, J.M., and Snurr, R.Q. (2021). Machine learning the quantum-chemical properties of metal–organic frameworks for accelerated materials discovery. Matter *4*, 1578–1597. https://doi.org/10.1016/j.matt.2021.02.015.

14. Ward, L., Liu, R., Krishna, A., Hegde, V.I., Agrawal, A., Choudhary, A., and Wolverton, C. (2017). Including crystal structure attributes in machine learning models of formation energies via Voronoi tessellations. Phys. Rev. B *96*, 024104. https://doi.org/10.1103/PHYSREVB.96.024104/FIGURES/8/MEDIUM.

15. Goodall, R.E.A., and Lee, A.A. (2020). Predicting materials properties without crystal structure: deep representation learning from stoichiometry. Nat. Commun. *11*, 6280. https://doi.org/10.1038/s41467-020-19964-7.

16. Noh, J., Kim, J., Stein, H.S., Sanchez-Lengeling, B., Gregoire, J.M., Aspuru-Guzik, A., Jung, Y., and Com, A. (2019). Inverse design of solid-state materials via a continuous representation. Matter *1*, 1370–1384. https://doi.org/10.1016/j.matt.2019.08.017.

17. Gómez-Bombarelli, R., Wei, J.N., Duvenaud, D., Hernández-Lobato, J.M., Sánchez-Lengeling, B., Sheberla, D., Aguilera-Iparraguirre, J., Hirzel, T.D., Adams, R.P., and Aspuru-Guzik, A. (2018). Automatic chemical design using a data-driven continuous representation of molecules. ACS Cent. Sci. *4*, 268–276. https://doi.org/10.1021/ACSCENTSCI.7B00572/SUPPL_FILE/OC7B00572_LIVESLIDES.MP4.

18. Yao, Z., Sánchez-Lengeling, B., Bobbitt, N.S., Bucior, B.J., Kumar, S.G.H., Collins, S.P., Burns, T., Woo, T.K., Farha, O.K., Snurr, R.Q., and Aspuru-Guzik, A. (2021). Inverse design of nanoporous crystalline reticular materials with deep generative models. Nat. Mach. Intell. *3*, 76–86. https://doi.org/10.1038/s42256-020-00271-1.

19. Kim, B., Lee, S., and Kim, J. (2020). Inverse design of porous materials using artificial neural networks. Sci. Adv. *6*. eaax9324. https://doi.org/10.1126/sciadv.aax9324.

20. Dan, Y., Zhao, Y., Li, X., Li, S., Hu, M., and Hu, J. (2020). Generative adversarial networks (GAN) based efficient sampling of chemical composition space for inverse design of inorganic materials. npj Comput. Mater. *6*, 84–87. https://doi.org/10.1038/s41524-020-00352-0.

21. Guimaraes, G., Sanchez-Lengeling, B., Outeiral, C., Luis, P., Farias, C., and Aspuru-Guzik, A. (2017). Objective-reinforced generative adversarial networks (ORGAN) for sequence generation models. Preprint at arXiv. https://doi.org/10.48550/arXiv.1705.10843.

22. Sanchez-Lengeling, B., Outeiral, C., Guimaraes, G.L., and Aspuru-Guzik, A. (2017). Optimizing distributions over molecular space. An objective-reinforced generative adversarial network for inverse-design chemistry (ORGANIC). Preprint at ChemRxiv. https://doi.org/10.26434/CHEMRXIV.5309668.V3.

23. Reeves, S., DiFrancesco, B., Shahani, V., MacKinnon, S., Windemuth, A., and Brereton, A.E. (2020). Assessing methods and obstacles in chemical space exploration. Appl. AI Lett. *1*, e17. https://doi.org/10.1002/AIL2.17.

24. Thiede, L.A., Krenn, M., Nigam, A., and Aspuru-Guzik, A. (2020). Curiosity in exploring chemical space: intrinsic rewards for deep molecular reinforcement learning. Preprint at arXiv. https://doi.org/10.48550/arXiv.2012.11293.

25. van de Walle, A. (2009). Multicomponent multisublattice alloys, nonconfigurational entropy and other additions to the Alloy Theoretic Automated Toolkit. Calphad *33*, 266–278. https://doi.org/10.1016/j.calphad.2008.12.005.

26. Blum, V., and Zunger, A. (2004). Mixed-basis cluster expansion for thermodynamics of bcc alloys. Phys. Rev. B *70*, 155108. https://doi.org/10.1103/PhysRevB.70.155108.

27. Nakayama, H., Koyama, J., Yoneoka, N., and Miyazawa, T. (2021). Description: third generation digital annealer technology. https://www.fujitsu.com/jp/documents/digitalannealer/researcharticles/DA_WP_EN_20210922.pdf.

28. Hong, S.W., Miasnikof, P., Kwon, R., and Lawryshyn, Y. (2021). Market graph clustering via QUBO and digital annealing. J. Risk Financ. Manag. *14*, 34.

29. Naghsh, Z., Javad-Kalbasi, M., and Valaee, S. (2019). Digitally annealed solution for the maximum clique problem with critical application in cellular V2X. In IEEE International Conference on Communications (Institute of Electrical and Electronics Engineers Inc.). https://doi.org/10.1109/ICC.2019.8761634.

30. Tran, R., Lan, J., Shuaibi, M., Goyal, S., Wood, B.M., Das, A., Heras-Domingo, J., Kolluru, A., Rizvi, A., Shoghi, N., et al. (2022). The open catalyst 2022 (OC22) dataset and challenges for oxide electrocatalysis. Preprint at arXiv. https://doi.org/10.48550/arxiv.2206.08917.

31. Batzner, S., Musaelian, A., Sun, L., Geiger, M., Mailoa, J.P., Kornbluth, M., Molinari, N., Smidt, T.E., and Kozinsky, B. (2022). E(3)-equivariant graph neural networks for data-efficient and accurate interatomic potentials. Nat. Commun. *13*, 2453. https://doi.org/10.1038/s41467-022-29939-5.

32. van de Walle, A., Asta, M., and Ceder, G. (2002). The alloy theoretic automated toolkit: a user guide. Calphad *26*, 539–553. https://doi.org/10.1016/S0364-5916(02)80006-2.

33. Blum, V., Hart, G.L.W., Walorski, M.J., and Zunger, A. (2005). Using genetic algorithms to map first-principles results to model Hamiltonians: application to the generalized Ising model for alloys. Phys. Rev. B *72*, 165113. https://doi.org/10.1103/PhysRevB.72.165113.

34. Paufler, P. (1992). F. Ducastelle. Order and phase stability in alloys. (Cohesion and structure Vol. 3). North-Holland/Elsevier science publishers, amsterdam 1991. 511 p. US $ 151./dfl. 295.00. ISBN 0–444–86973–5. The book is available either from the amsterdam address or from Elsevier Sc. Publ. New York. Cryst. Res. Technol. *27*, 874. https://doi.org/10.1002/crat.2170270624.

35. Sanchez, J.M., Ducastelle, F., and Gratias, D. (1984). Generalized cluster description of multicomponent systems. Phys. Stat. Mech. Appl. *128*, 334–350. https://doi.org/10.1016/0378-4371(84)90096-7.

36. Li, C., Nilson, T., Cao, L., and Mueller, T. (2021). Predicting activation energies for vacancy-mediated diffusion in alloys using a transition-state cluster expansion. Phys. Rev. Mater. *5*. 013803. https://doi.org/10.1103/PhysRevMaterials.5.013803.

37. Mueller, T., and Ceder, G. (2009). Bayesian approach to cluster expansions. Phys. Rev. B *80*. 024103. https://doi.org/10.1103/PhysRevB.80.024103.

38. Ozoliņš, V., Wolverton, C., and Zunger, A. (1998). Cu-Au, Ag-Au, Cu-Ag, and Ni-Au intermetallics: first-principles study of temperature-composition phase diagrams and structures. Phys. Rev. B *57*, 6427–6443. https://doi.org/10.1103/PhysRevB.57.6427.

39. Blum, V., Hart, G., Richter, N., Hart, G.L.W., Rosenbrock, C.W., Bieniek, B., et al. (2014). Hands-On Tutorial on Cluster Expansion Modeling of Configurational Energetics Manuscript for Exercise Problems Adapted from a Tutorial Originally Prepared by V. Blum.

40. Babbush, R., Perdomo-Ortiz, A., O'gorman, B., Macready, W., and Aspuru-Guzik, A. (2013). Construction of energy functions for lattice heteropolymer models: a case study in constraint satisfaction programming and adiabatic quantum optimization. Preprint at arXiv. https://doi.org/10.48550/arXiv.1211.3422.

41. Kim, D.W., Park, Y.J., Moon, J.W., Ryi, S.K., and Park, J.S. (2008). The effect of Cu reflow on the Pd–Cu–Ni ternary alloy membrane fabrication for infinite hydrogen separation. Thin Solid Films *516*, 3036–3044. https://doi.org/10.1016/J.TSF.2007.11.126.

42. Feng, Y., Shao, Q., Ji, Y., Cui, X., Li, Y., Zhu, X., and Huang, X. (2018). Surface-modulated palladium-nickel icosahedra as high-performance non-platinum oxygen reduction electrocatalysts. Sci. Adv. *4*. eaap8817. https://doi.org/10.1126/SCIADV.AAP8817.

43. Lin, Y., Tian, Z., Zhang, L., Ma, J., Jiang, Z., Deibert, B.J., Ge, R., and Chen, L. (2019). Chromium-ruthenium oxide solid solution electrocatalyst for highly efficient oxygen evolution reaction in acidic media. Nat. Commun. *10*, 162. https://doi.org/10.1038/s41467-018-08144-3.

44. Teeriniemi, J., Taskinen, P., and Laasonen, K. (2015). First-principles investigation of the Cu–Ni, Cu–Pd, and Ni–Pd binary alloy systems. Intermetallics *57*, 41–50. https://doi.org/10.1016/J.INTERMET.2014.09.006.

45. Fortin, F.-A., De Rainville, F.-M., Gardner, M.-A.G., Parizeau, M., and Gagné, C. (2012). DEAP: evolutionary algorithms made easy. J. Mach. Learn. Res. *13*, 2171–2175.

Matter
Article

<img> CellPress

46. Head, T., MechCoder, Louppe, G., Shcherbatyi, I., fcharras, Vinícius, Z., cmmalone, Schröder, C., nel215, Campos, N., et al. (2018). scikit-optimize/scikit-optimize: v0.5.2. https://doi.org/10.5281/ZENODO.1207017.

47. Shi, Z., Wang, X., Ge, J., Liu, C., and Xing, W. (2020). Fundamental understanding of the acidic oxygen evolution reaction: mechanism study and state-of-the-art catalysts. Nanoscale 12, 13249–13275. https://doi.org/10.1039/d0nr02410d.

48. Hu, C., Zhang, L., and Gong, J. (2019). Recent progress made in the mechanism comprehension and design of electrocatalysts for alkaline water splitting. Energy Environ. Sci. 12, 2620–2645. https://doi.org/10.1039/c9ee01202h.

49. Seitz, L.C., Dickens, C.F., Nishio, K., Hikita, Y., Montoya, J., Doyle, A., Kirk, C., Vojvodic, A., Hwang, H.Y., Norskov, J.K., and Jaramillo, T.F. (2016). A highly active and stable IrOx/SrIrO3catalyst for the Oxygen evolution reaction. Science 353, 1011–1014. https://doi.org/10.1126/science.aaf5050.

50. Yang, L., Yu, G., Ai, X., Yan, W., Duan, H., Chen, W., Li, X., Wang, T., Zhang, C., Huang, X., et al. (2018). Efficient oxygen evolution electrocatalysis in acid by a perovskite with face-sharing IrO6 octahedral dimers. Nat. Commun. 9, 5236. https://doi.org/10.1038/s41467-018-07678-w.

51. Zhang, B., Wang, L., Cao, Z., Kozlov, S.M., García de Arquer, F.P., Dinh, C.T., Li, J., Wang, Z., Zheng, X., Zhang, L., et al. (2020). High-valence metals improve oxygen evolution reaction performance by modulating 3d metal oxidation cycle energetics. Nat. Catal. 3, 985–992. https://doi.org/10.1038/s41929-020-00525-6.

52. Gou, W., Zhang, M., Zou, Y., Zhou, X., and Qu, Y. (2019). Iridium-chromium oxide nanowires as highly performed OER catalysts in acidic media. ChemCatChem 11, 6008–6014. https://doi.org/10.1002/cctc.201901411.

53. Dionigi, F., and Strasser, P. (2016). NiFe-based (Oxy)hydroxide catalysts for oxygen evolution reaction in non-acidic electrolytes. Adv. Energy Mater. 6. 1600621. https://doi.org/10.1002/aenm.201600621.

54. Li, L., Wang, P., Shao, Q., and Huang, X. (2021). Recent progress in advanced electrocatalyst design for acidic oxygen evolution reaction. Adv. Mater. 33. e2004243. https://doi.org/10.1002/adma.202004243.

55. Hammer, B., and Nørskov, J. (2000). Theoretical surface science and catalysis—calculations and concepts. Adv. Catal. 45, 71–129. https://doi.org/10.1016/S0360-0564(02)45013-4.

56. Hammer, B., and Norskov, J.K. (1995). Why gold is the noblest of all the metals. Nature 376, 238–240. https://doi.org/10.1038/376238a0.

57. Hammer, B., and Nørskov, J. (1995). Electronic factors determining the reactivity of metal surfaces. Surf. Sci. 343, 211–220. https://doi.org/10.1016/0039-6028(96)80007-0.

58. Nilsson, A., Pettersson, L.G.M., and Nørskov, J.K.. Chemical Bonding at Surfaces and Interfaces. https://www.elsevier.com/books/chemical-bonding-at-surfaces-and-interfaces/nilsson/978-0-444-52837-7. First edition.

59. Liu, J., Liu, H., Chen, H., Du, X., Zhang, B., Hong, Z., Sun, S., and Wang, W. (2020). Progress and challenges toward the rational design of oxygen electrocatalysts based on a descriptor approach. Adv. Sci. 7. 1901614. https://doi.org/10.1002/ADVS.201901614.

60. Pedersen, J.K., Clausen, C.M., Krysiak, O.A., Xiao, B., Batchelor, T.A.A., Löffler, T., Mints, V.A., Banko, L., Arenz, M., Savan, A., et al. (2021). Bayesian optimization of high-entropy alloy compositions for electrocatalytic oxygen reduction. Angew. Chem. Int. Ed. Engl. 60, 24144–24152. https://doi.org/10.1002/ANIE.202108116.

61. Zhang, B., Zheng, X., Voznyy, O., Comin, R., Bajdich, M., García-Melchor, M., Han, L., Xu, J., Liu, M., Zheng, L., et al. (2016). Homogeneously dispersed, multimetal oxygen-evolving catalysts. Science 352, 333–337. https://doi.org/10.1126/science.aaf1525.

62. Wen, Y., Chen, P., Wang, L., Li, S., Wang, Z., Abed, J., Mao, X., Min, Y., Dinh, C.T., Luna, P.D., et al. (2021). Stabilizing highly active Ru sites by suppressing lattice oxygen participation in acidic water oxidation. J. Am. Chem. Soc. 143, 6482–6490. https://doi.org/10.1021/jacs.1c00384.

63. Sorantin, P.I., and Schwarz, K. (2002). Chemical bonding in rutile-type compounds. Inorg. Chem. 31, 567–576. https://doi.org/10.1021/IC00030A009.

64. Wang, X., Yang, M., Feng, W., Qiao, L., An, X., Kong, Q., Liu, X., Wang, Y., Liu, Y., Li, T., et al. (2021). Significantly enhanced oxygen evolution reaction performance by tuning surface states of Co through Cu modification in alloy structure 903. 115823. https://doi.org/10.1016/J.JELECHEM.2021.115823.

65. Yuge, K. (2012). Modeling configurational energetics on multiple lattices through extended cluster expansion. Phys. Rev. B 85. 144105. https://doi.org/10.1103/PHYSREVB.85.144105/FIGURES/5/MEDIUM.

66. Jain, A., Ong, S.P., Hautier, G., Chen, W., Richards, W.D., Dacek, S., Cholia, S., Gunter, D., Skinner, D., Ceder, G., and Persson, K.A. (2013). Commentary: the materials project: a materials genome approach to accelerating materials innovation. Apl. Mater. 1. 011002. https://doi.org/10.1063/1.4812323.

67. Perdew, J.P., Burke, K., and Ernzerhof, M. (1996). Generalized gradient approximation made simple. Phys. Rev. Lett. 77, 3865–3868. https://doi.org/10.1103/PhysRevLett.77.3865.

68. Ångqvist, M., Muñoz, W.A., Rahm, J.M., Fransson, E., Durniak, C., Rozyczko, P., Rod, T.H., and Erhart, P. (2019). ICET – a Python library for constructing and sampling alloy cluster expansions. Adv. Theory Simul. 2. 1900015. https://doi.org/10.1002/ADTS.201900015.

69. Gurobi Optimization, LLC (2022). Gurobi Optimizer Reference Manual (Gurobi Optimization, LLC).